J Adv Ceram

Research Article

Ultra-fast synthesis and composition-dependent formation behavior of $(Hf_xZr_{1-x})B_2$ solid solution nanopowders

Sen Yang[1,2,†], Zhengang Zhang[1,†], Yanqin Fu[1,✉], Tao Li[1], Liyuan Han[1], Lingxiang Guo[3], Hang Yu[3], Jianhua Zhang[1], Wei Xie[2], Hailong Wang[2], Yulei Zhang[1,3,✉]

Cite this article: Yang S, Zhang Z, Fu Y, et al. *J Adv Ceram* 2026, **15**(5): 9221284. https://doi.org/10.26599/JAC.2026.9221284

ABSTRACT: Ultrafine boride solid solutions offer immense potential for extreme environmental applications, yet their rapid synthesis with nanoscale compositional control remains a challenge. Herein, we exploit ultrafast high-temperature sintering to achieve the rapid synthesis of a $(Hf_xZr_{1-x})B_2$ solid solution with exceptional nanoscale homogeneity. The phase composition and evolution during solid solution formation, as well as the formation tendency with varying Hf/Zr molar ratios, were systematically investigated. First-principles calculations reveal a progressively enhanced tendency to form a single-phase solid solution with increasing Hf content, which is attributed to the lower solution energy (E_{sol}) for Zr atoms incorporating into the HfB_2 lattice compared with the reverse process. This finding is consistent with the result of a lower synthesis temperature for $(Hf_{0.8}Zr_{0.2})B_2$ (1700 °C). In addition, $(Hf_{0.8}Zr_{0.2})B_2$ also exhibits superior phase and thermodynamic stability, as demonstrated by its more negative ΔG_{mix}, lower DOS value at E_f, and reduced average bond length. This work not only establishes an efficient pathway for powder synthesis but also delivers foundational insights for the rational design of multidiboride ceramics.

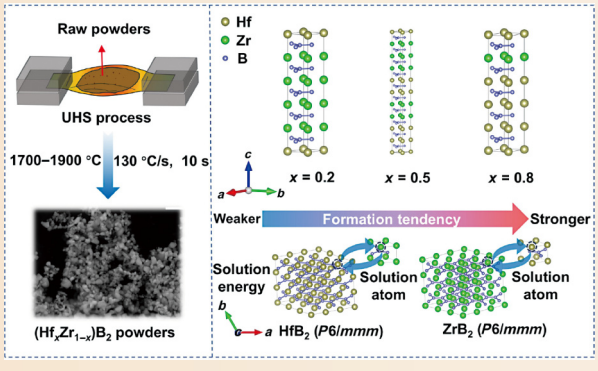

KEYWORDS: ultrafine; ultrafast high-temperature sintering; solid solution; formation tendency

1 Introduction

Ultrahigh temperature ceramics (UHTCs), primarily including refractory transition metal borides (HfB_2, ZrB_2, TaB_2, TiB_2, etc.), carbides (HfC, ZrC, TaC, etc.) and nitrides (HfN, TaN, etc.), are characterized by their ultrahigh melting points (exceeding 3000 °C), exceptional ablative resistance and high thermal conductivity, making them highly suitable as high-temperature structural materials for hypersonic aerospace vehicles [1–7]. Among them, borides such as HfB_2 and ZrB_2 exhibit high thermal conductivity and superior oxidation and ablation resistance compared to their carbide and nitride counterparts [8–13].

Owing to the same crystal structure (hexagonal, space group *P6/mmm*) and similar lattice parameters, ZrB_2 and HfB_2 can form continuous $(Hf,Zr)B_2$ solid solutions across the entire compositional range [14,15]. Efforts have confirmed that such solid solutions outperform the individual diborides in mechanical properties and oxidation/ablation resistance. For instance, $(Hf_{0.5}Zr_{0.5})B_2$ exhibited improved densification behavior and oxidation resistance [16]. Furthermore, mechanical properties, including hardness [17], fracture toughness, and flexural strength, can be tailored and enhanced through controlling the Hf/Zr molar ratio, as demonstrated in $(Hf_xZr_{1-x})B_2$–SiC composites [18]. The strategy of multicomponent solid solution has been extended to even more complex systems, such as equimolar $(Hf–Zr–Ta–Ti)B_2$ coatings, which yielded improved results for the ablation protection of C/C composites [19]. These improved properties underscore the necessity for developing efficient and scalable synthesis routes to high-quality boride solid solution powders. Crucially, achieving nanoscale compositional control in such solid solutions is particularly important, as it directly governs key performance metrics, including enhanced sinterability due to higher surface energy and diffusion rates [20], optimized mechanical properties (e.g., hardness, fracture toughness) through grain boundary strengthening and defect engineering [21], and superior oxidation/ablation resistance by enabling the formation of more uniform and protective oxide scales [22].

† Sen Yang and Zhengang Zhang contributed equally to this work.

[1] Henan Key Laboratory of High Performance Carbon Fiber Reinforced Composites, Institute of Carbon Matrix Composites, Henan Academy of Sciences, Zhengzhou 450046, China. [2] School of Materials Science and Engineering, Zhengzhou University, Zhengzhou 450001, China. [3] Shaanxi Key Laboratory of Fiber Reinforced Light Composite Materials, Northwestern Polytechnical University, Xi'an 710072, China.

✉ Corresponding authors. E-mail: Y. Fu, fuyanqin@hnas.ac.cn; Y. Zhang, zhangyulei@nwpu.edu.cn

Received: November 20, 2025; Revised: February 14, 2026; Accepted: March 17, 2026

Conventional powder synthesis methods, including high-energy ball milling [23], self-propagating high-temperature synthesis [24] and sol-gel processing [25], often face challenges related to prolonged processing time, incomplete reaction or inadequate control over powder homogeneity and coarsening [8]. The recent emergence of ultrafast high-temperature sintering (UHS), pioneered by Hu *et al.* [26], utilizes Joule heating of raw material powders encapsulated within graphite paper to achieve ultrafast heating rates (up to 10^4 °C/min) and extreme temperatures (up to 3000 °C). By effectively bypassing low-temperature regimes, where particle coarsening typically occurs, UHS enables the rapid synthesis of ultrafine and high-purity ceramic powders. Owing to the above advantages, the potential for high-throughput exploration of complex ceramic systems, including multication diborides and high-entropy borides, is rapidly being recognized [27]. For instance, Tang *et al.* [28] synthesized equimolar 1- to 9-cation multicomponent diborides of the IVB, VB, and VIB groups in seconds via the UHS technique, investigating the oxidation resistance of high-entropy boride ceramics. Despite these advancements, current research on equimolar/nonequimolar boride solid solution ceramic systems generally prioritizes macroproperty reporting over a fundamental analysis of solid solution behavior [29,30]. The essential phase evolution pathways and atomic-scale diffusion kinetics that govern the formation and final properties of these solid solutions remain insufficiently explored.

In this work, we report the ultrafast synthesis of $(Hf_xZr_{1-x})B_2$ (x = 0.2, 0.5, and 0.8) solid solution nanopowders via a borothermal reduction reaction. This approach achieves complete solid solution formation within a remarkably short duration of 10 s at 1700–1900 °C. Compared with conventional heat treatment methods [31], the UHS process effectively suppresses grain growth by limiting atomic diffusion due to its ultrashort processing duration, thereby maintaining nanoscale particles. The morphology, particle size and phase evolution were systematically investigated. Furthermore, first-principles calculations were employed to conduct an in-depth analysis of the phase stability across different compositions and to elucidate the diffusion behavior of Hf and Zr species during dissolution. This combined theoretical and experimental work provides a foundation for the rational design and application of multicomponent boride ceramics in extreme environments.

2 Experimental

2.1 Powder Synthesis

Figure 1 shows a schematic diagram of the UHS process of $(Hf_xZr_{1-x})B_2$ powders. Commercial HfO_2, ZrO_2, and amorphous B powders (99.9% purity, 200 nm, Shanghai ChaoWei Nanotechnology Co., Ltd., China) were used as raw materials. Three compositions with Hf/Zr molar ratios of 1 : 4, 1 : 1, and 4 : 1 were designed, corresponding to x = 0.2, 0.5, and 0.8 in $(Hf_xZr_{1-x})B_2$, and were denoted as HZ4, HZ, and H4Z, respectively. The precursor powders were mixed and ball-milled in ethanol using agate balls as the media. After being sieved through a 50-mesh screen, the mixed powders were wrapped in graphite paper and placed between two metal clips. Then, the device was vacuumed to below −0.1 MPa. Subsequently, the alternating current was applied directly through the graphite paper to heat the raw materials to the desired temperature at an extremely high heating rate. A linear heating rate of 130 °C/s was applied for all target temperatures (1700–1900 °C), followed by an isothermal hold of 10 s. After the heating process, the power was switched off to naturally cool to room temperature. The temperature was monitored *in situ* using an infrared thermometer focused on the surface of graphite paper. The reactions that occur during the process are listed as Eq. (1) [32]:

$$xHfO_2 + (1-x)ZrO_2 + 10/3B = (Hf_xZr_{1-x})B_2 + 2/3B_2O_3 \quad (1)$$

2.2 Computational details

All first-principles calculations were carried out within the framework of density functional theory (DFT) as implemented in the Vienna *Ab initio* simulation package (VASP) using the plane-wave pseudopotential approach [33]. The electron exchange-correlation interactions were treated with the generalized gradient approximation (GGA) in the Perdew–Burke–Ernzerhof (PBE) parametrization [34,35]. The cutoff energy used in the calculation is 500 eV, with valence electron configurations of $5d^26s^2$, $4d^25s^2$, and $2s^22p^1$ for Hf, Zr and B, respectively. Solid-solution structures were modeled using 1 × 1 × 5 supercells for $(Hf_{0.2}Zr_{0.8})B_2$ (a = 3.168 Å, c = 17.715 Å) and $(Hf_{0.8}Zr_{0.2})B_2$ (a = 3.149 Å, c = 17.514 Å) with a 10 × 10 × 2 k-mesh and a 1 × 1× 10 supercell for $(Hf_{0.5}Zr_{0.5})B_2$ (a = 3.159 Å, c = 35.231 Å) with a 10 × 10 × 1

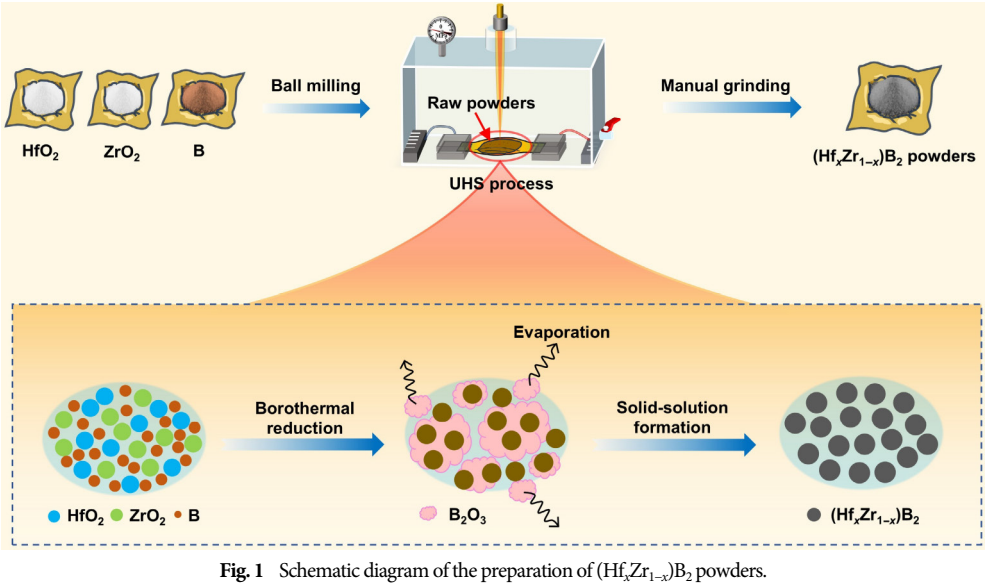

Fig. 1 Schematic diagram of the preparation of $(Hf_xZr_{1-x})B_2$ powders.

k-mesh. Structural optimizations were considered converged when the total energy difference fell below 1×10^{-7} eV/atom and the maximum force was less than 0.01 eV/Å.

2.3 Characterizations of $(Hf_xZr_{1-x})B_2$ ceramic powders

The phase compositions and lattice parameters of $(Hf_xZr_{1-x})B_2$ prepared by the UHS process were determined by an X-ray diffractometer (XRD; Empyrean, Malvern PANalytical, the Netherlands) analysis with Cu Kα radiation. The morphology and microstructure of the ceramic powders were characterized by a field-emission scanning electron microscope (FESEM; GeminiSEM 360, ZEISS, Germany) and a transmission electron microscope (TEM; Talos F200x, Thermo Fisher Scientific, USA) equipped with EDS. The average particle size was measured using a dynamic light scattering instrument (DLS; Zetasizer Pro, Malvern PANalytical, UK). The oxygen content was determined by an oxygen-nitrogen-hydrogen analyzer (ONH 836, Leco, USA).

3 Results and discussion

3.1 Phase evolution and solid solution formation during the UHS process

Figure 2 shows the XRD patterns of the synthesized $(Hf_xZr_{1-x})B_2$ ceramic powders using the UHS technique. As presented in Figs. 2(a), 2(d), and 2(g), across all compositions (HZ4, HZ, H4Z), secondary boride phases were detected until a critical temperature was achieved. Specifically, Hf-rich secondary phases (named HS) were observed in HZ4 and HZ, and Zr-rich secondary phases (named ZS) were observed in HZ and H4Z. The minimum temperature required to achieve a phase-pure solid solution was found to be composition dependent. Single-phase $(Hf_{0.8}Zr_{0.2})B_2$ and $(Hf_{0.5}Zr_{0.5})B_2$ solid solutions (AlB_2 structure with a space group of *P6/mmm*) formed at 1700 and 1800 °C, respectively. In contrast, the single-phase solid solution for $(Hf_{0.2}Zr_{0.8})B_2$ required a higher temperature of 1900 °C. This trend demonstrates that the formation tendency strengthens with increasing Hf content, with the dissolution of Hf-rich phases into a Zr-rich matrix presenting a greater kinetic barrier. The evolution of the (101) diffraction peak provides further macroscopic insight into the dissolution process. As shown in the enlarged image of Figs. 2(a), 2(d), and 2(g), the peak of solid solution $(Hf_xZr_{1-x})B_2$ shifts to higher angles with increasing Hf content due to the decrease in the lattice parameters induced by Hf substitution.

More specifically, for HZ4 in Fig. 2(a), as the heat treatment temperature increased from 1300 to 1800 °C, HS coexisted with the main solid solution phase (denoted as SS1), as indicated by the (101) diffraction peak in the partially enlarged view. The continuous increased intensity and slight rightward shift of the SS1 peak below 1900 °C demonstrate the progressive diffusion of HS into SS1, refining its average composition toward $(Hf_{0.2}Zr_{0.8})B_2$ and reducing its lattice parameters. For equimolar HZ (Fig. 2(d)), both HS and ZS coexist from 1300 to 1700 °C, and the mutual diffusion between these two secondary phases leads to a gradual

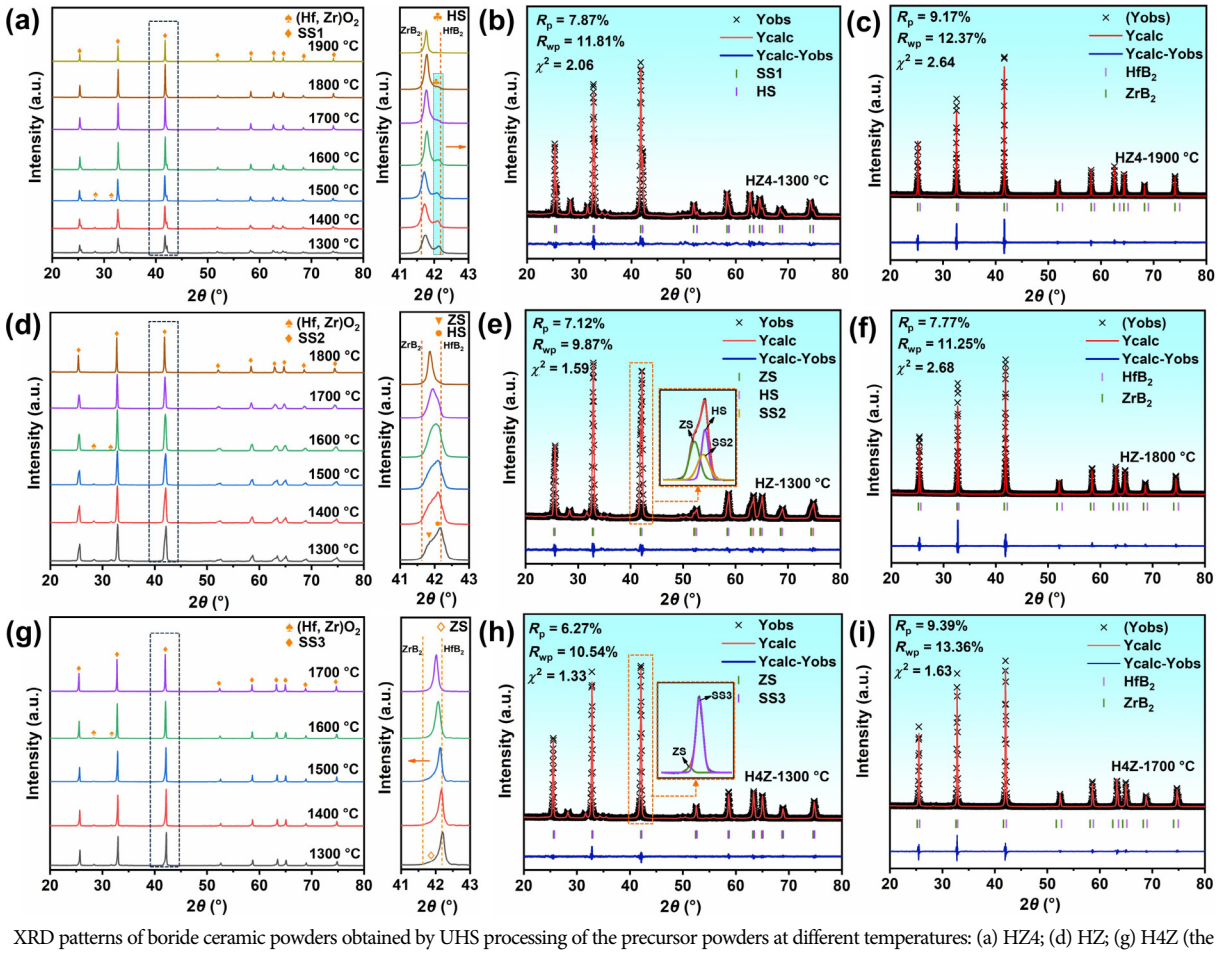

Fig. 2 XRD patterns of boride ceramic powders obtained by UHS processing of the precursor powders at different temperatures: (a) HZ4; (d) HZ; (g) H4Z (the partial enlargement of the (101) diffraction peaks correspond to the area enclosed by the dashed rectangle); (b, e, h) ceramic powders obtained at 1300 °C (the inset shows the deconvoluted (101) peak), and (c, f, i) single-phase solid solution boride ceramic powders with three distinct compositions along with Rietveld refinement.

increase in the intensity of the main solid solution phase (denoted as SS2). Upon reaching 1800 °C, the enhanced dissolution and diffusion results in a homogeneous single-phase solid solution, corresponding to $(Hf_{0.5}Zr_{0.5})B_2$, with lattice parameters intermediate between those of ZrB_2 and HfB_2. For H4Z (Fig. 2(g)), the dissolution of ZS into the main solid solution phase (denoted as SS3) resulted in a continuous shift of the diffraction peaks toward lower angles from 1300 to 1600 °C.

For further investigation of the phase evolution, multiphase Rietveld refinement was conducted on partial powders synthesized at 1300 °C. The refinement results, as depicted in Figs. 2(b), 2(e), and 2(h), confirm the multiphase feature at this intermediate stage. The HZ4-1300 °C consists of a primary SS1 (near to composition of $(Hf_{0.2}Zr_{0.8})B_2$) along with HS. Conversely, H4Z-1300 °C contains a primary SS3 (near to the composition of the $(Hf_{0.8}Zr_{0.2})B_2$) and ZS phases (Fig. 2(h)). Notably, the equimolar HZ exhibits a distinct pathway (Fig. 2(e)), characterized by the coexistence of both HS and ZS phases, which gradually interdiffuse to form SS2 followed by a final homogeneous solid solution. The insets in Figs. 2(e) and 2(h) present the deconvolution of the (101) peak, with each subpeak assigned to the boride main solid solution phase and its secondary phases, in good agreement with the XRD refinement results.

To further investigate the phase evolution trends during the solid solution process, Rietveld refinement of XRD patterns was also conducted on powders treated at 1500 °C. To avoid introducing excessive variables that could affect the fitting effect, and given that the residual oxide phase is minor, the oxide peaks were excluded during the Rietveld refinement of the XRD patterns. Only the boride main solid solution phase and its secondary phases were refined, and the weight fractions (V) of the boride phases were directly obtained from the refinement results. The weight fraction of the residual oxide phase was separately calculated using Klug's equation (Eq. (2)) [36]:

$$V = \frac{\left(\frac{I_1^{\text{mix}}}{I_1^{\text{pure}}}\right) A_2}{A_1 - \left(\frac{I_1^{\text{mix}}}{I_1^{\text{pure}}}\right)(A_1 - A_2)} \quad (2)$$

where I_1^{mix} and I_1^{pure} are the intensities of $(Hf_xZr_{1-x})O_2$ (x = 0.2, 0.5, 0.8) in the mixture and pure material, respectively, and A_1 and A_2 are the mass absorption coefficients of the residual oxide phase $(Hf_xZr_{1-x})O_2$ and the corresponding boride phase $(Hf_xZr_{1-x})B_2$, respectively. Since the oxide phase was not included in the refinement, normalization was applied to obtain relatively accurate weight fractions. The weight fractions and lattice parameters of each phase are listed in Table 1. At the same heating temperature, HZ4, HZ and H4Z exhibit sequentially diminishing weight fractions of residual oxides, which quantitatively reflects the progressively enhanced solid solution process (HZ4 < HZ < H4Z). These results are consistent with the phase evolution trends observed in Figs. 2(a), 2(d), and 2(g).

As the temperature increased from 1300 to 1500 °C, the weight fraction of HS in HZ4 and ZS in H4Z progressively decreased, confirming their ongoing dissolution into SS1 and SS3, respectively. The lattice parameters (a = 3.144–3.146 Å, c = 3.481–3.483 Å) of HS in HZ4 closely match those of $(Hf_{0.8}Zr_{0.2})B_2$. For HZ, notably, the concurrent decline in the weight fractions of HS and ZS alongside the increasing weight fraction of SS2 suggests diffusion and dissolution between the two phases, ultimately forming a stoichiometric $(Hf_{0.5}Zr_{0.5})B_2$ solid solution. The weight fraction of ZS showed a more pronounced decrease (40.0%) than that of HS (23.9%) as the temperature increased from 1300 to 1500 °C, confirming that the dissolution of the Zr-rich phase into the Hf-rich matrix exhibits a higher tendency than the reverse process. The lattice parameters of ZS (a = 3.157–3.159 Å, c = 3.511–3.157 Å) are intermediate between $(Hf_{0.2}Zr_{0.8})B_2$ and $(Hf_{0.5}Zr_{0.5})B_2$, with its composition back-calculated as $(Hf_{0.28-0.36}Zr_{0.64-0.72})B_2$ via Vegard's law, and the composition of HS was close to $(Hf_{0.8}Zr_{0.2})B_2$ with lattice parameters a = 3.143–3.144 Å, c = 3.479–3.480 Å. For H4Z, the composition was estimated by back-calculating from the lattice parameters of ZS (a = 3.152–3.156 Å, c = 3.493–3.499 Å) as $(Hf_{0.55-0.65}Zr_{0.35-0.45})B_2$.

Finally, Rietveld refinement was employed to characterize the crystal structure of the final single-phase solid solution using a hexagonal cell with the *P6/mmm* space group. Representative XRD patterns along with their Rietveld refinement are presented in Figs. 2(c), 2(f), and 2(i), with fitting parameter values confirming the high reliability of the structural models for all $(Hf_xZr_{1-x})B_2$ compositions. The synthesized powders possess a well-defined hexagonal phase.

The formation of secondary phases during solid solution evolution was further investigated by TEM, with HZ-1300 °C powders utilized as the representative case. The elemental mapping in Figs. 3(a) and 3(b) reveals localized Zr-rich (area 1) and Hf-rich (area 2) regions, which are attributed to HS and ZS identified by XRD in Fig. 2(d). HRTEM images combined by fast Fourier transform (FFT) analysis of Areas 1 and 2 indexed along the $[\bar{1}0\bar{1}]$ and $[\bar{1}00]$ zone axes (Figs. 3(f) and 3(g)), confirming that both secondary phases exhibit an AlB_2-type hexagonal structure, which is a typical characteristic of borides. The SS2 phase can also

Table 1 Summary of the contents and lattice parameters of each phase in $(Hf_xZr_{1-x})B_2$

Phase		Heat treatment temperature (°C)	Weight fraction (%)	a (Å)	c (Å)
HZ4	SS1	1300	79.1	3.165–3.166	3.522
		1500	85.4		
	HS	1300	8.7	3.144–3.146	3.481–3.483
		1500	8.0		
	$(Hf,Zr)O_2$	1300	12.2	—	—
		1500	6.6		
HZ	SS2	1300	20.1	3.147–3.152	3.492–3.497
		1500	43.7		
	HS	1300	33.0	3.143–3.144	3.479–3.480
		1500	25.1		
	ZS	1300	41.2	3.157–3.159	3.511–3.517
		1500	28.7		
	$(Hf,Zr)O_2$	1300	5.7	—	—
		1500	2.5		
H4Z	SS3	1300	87.4	3.143–3.146	3.479–3.483
		1500	93.9		
	ZS	1300	8.5	3.152–3.156	3.493–3.499
		1500	5.1		
	$(Hf,Zr)O_2$	1300	4.1	—	—
		1500	1.0		
$(Hf_{0.2}Zr_{0.8})B_2$		—	—	3.164	3.517
$(Hf_{0.4}Zr_{0.6})B_2$		—	—	3.160	3.500
$(Hf_{0.5}Zr_{0.5})B_2$		—	—	3.154	3.495
$(Hf_{0.8}Zr_{0.2})B_2$		—	—	3.145	3.481

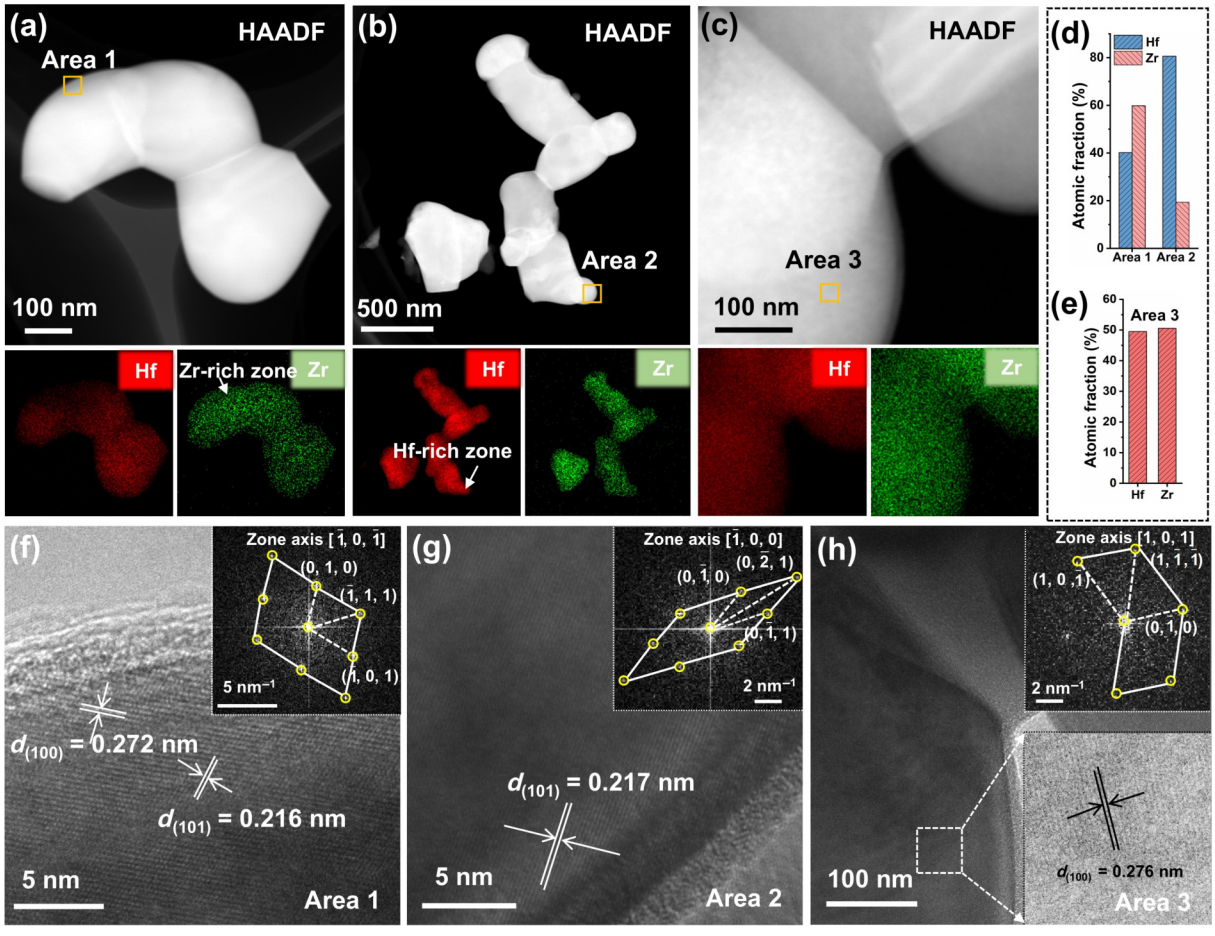

Fig. 3 TEM analysis of the HZ-1300 °C solid solution powders: (a–c) HADDF image and corresponding element mapping of HZ-1300 °C ceramic powders by UHS technology; (d, e) EDS quantitation of areas 1, 2 and 3; (f–h) HRTEM of areas 1, 2, 3 and corresponding fast Fourier transform images.

be identified from the TEM images (Figs. 3(c) and 3(h)), which is consistent with the XRD patterns in Figs. 2(d) and 2(e). Quantitative EDS analysis reveals distinct compositions. In region 1, the atomic fractions of Hf and Zr are 40.16% and 59.84%, respectively. In region 2, the corresponding values are 80.61% and 19.39%, while in region 3, they are 49.47% and 50.53%, respectively. These atomic ratios are close to the calculated or theoretical compositions of the ZS, HS, and SS2 phases and are consistent with the XRD Rietveld refinement results.

3.2 Microstructure and compositional characteristics of the nanopowders

The microstructural evolution of the $(Hf_xZr_{1-x})B_2$ powders synthesized via the UHS process was characterized by SEM in Fig. 4. The average particle size of the HZ ceramic powders increases from 323.1 to 451.7 nm as the heat treatment temperature gradually increases, as evidenced by Figs. 4(a), 4(b), and 4(d). Based on Fig. 2, heat treatment temperatures were selected as 1900 °C for HZ4, 1800 °C for HZ and 1700 °C for H4Z precursor powders to ensure the formation of homogeneous single-phase boride solid solutions. Figures 4(c)–4(e) reveal that HZ4-1900 °C exhibits a relatively larger average particle size (~485.9 nm) due to its higher processing temperatures. The EDS results confirm a homogeneous elemental distribution in all three compositions.

Detailed nanostructural analysis was performed on the representative HZ-1800 °C powders, and the HAADF image and EDS elemental mapping (Fig. 5(a)) demonstrate a uniform distribution of Hf and Zr at the nanoscale, indicating the formation of a chemically homogeneous solid solution. The HRTEM image (Fig. 5(b)) reveals lattice fringes of 0.216 and 0.274 nm, corresponding to the (101) and (100) crystallographic planes, respectively. An amorphous B_2O_3 layer with a thickness of 2–3 nm was observed on the surface of the synthesized powders, in accordance with Ref [37]. Sintered bulk ceramic samples were used for oxygen content analysis by ONH analyzer, yielding a value of 0.0055 wt%, which indirectly indicates that the oxygen content of the as-synthesized powders is also expected to be at a relatively low level. The SAED pattern along the [211] zone axis (Fig. 5(c)) further confirms the well-defined crystal structure and the absence of a secondary phase. The corresponding EDS quantitation (Fig. 5(d)) indicates that the atomic fractions of Hf and Zr are 51.95% and 48.05%, respectively, in good agreement with the stoichiometry of $(Hf_{0.5}Zr_{0.5})B_2$. The above results collectively verify the successful synthesis of binary solid solution powders with the expected $(Hf_{0.5}Zr_{0.5})B_2$ compositions.

3.3 Forming tendency and stability analysis of single-phase solid solutions

DFT calculations were employed to gain fundamental insights into the stability and formation tendency of the $(Hf_xZr_{1-x})B_2$ solid solution. To address stochastic variation in model building, five randomized configurations were generated by introducing the Shuffle function to achieve atomic disorder between Hf and Zr atoms, and the structure with the lowest energy after DFT relaxation was selected for subsequent property calculations [38].

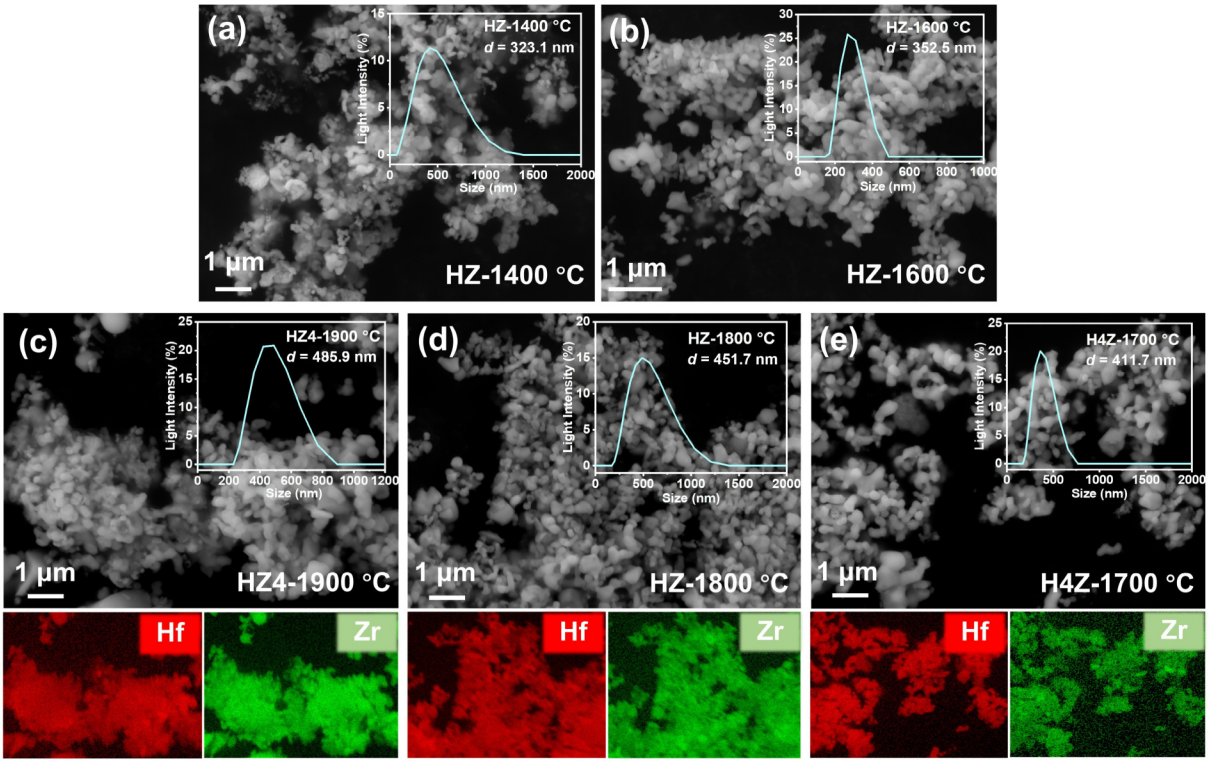

Fig. 4 Microscopic morphology of ceramic powders obtained by UHS technology: (a) HZ-1400 °C; (b) HZ-1600 °C; (c–e) HZ4-1900 °C, HZ-1800 °C, H4Z-1700 °C and corresponding EDS mappings. The inset in the upper-right corner of the SEM image shows the particle size distribution obtained by laser particle size analysis.

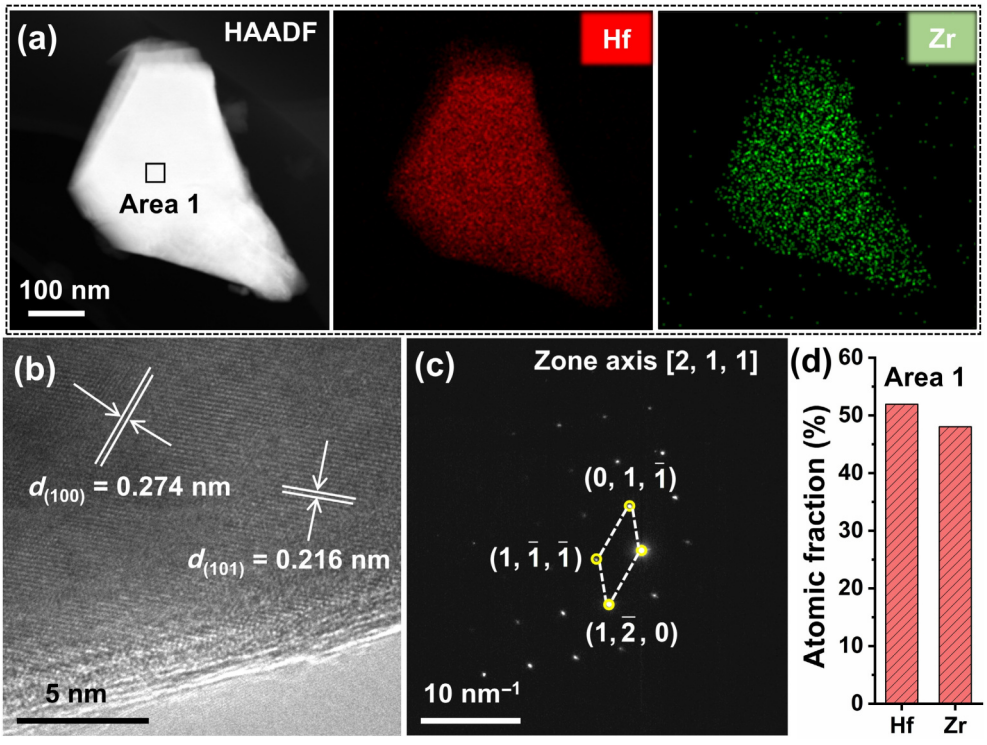

Fig. 5 TEM analysis of the as-synthesized HZ-1800 °C solid solution powders: (a) HAADF image together with EDS mapping; (b) HRTEM image; (c) SAED pattern; (d) EDS quantitation corresponding to the partially enlarged image (i.e., area 1) in (a).

The corresponding lattice parameters obtained from DFT structural optimization are summarized in Table 2. The parameter δ is commonly employed to assess the formation feasibility of solid solutions. For a multicomponent diboride system, δ is defined as Eq. (3) [39]:

$$\delta = \sqrt{\sum_{i=1}^{n} x_i \left(1 - \frac{r_i}{\bar{r}}\right)^2} \quad (3)$$

where n is the number of constituent borides in solid solution. x_i and r_i are the molar fraction and lattice parameters of the i-th

Table 2 Calculated ΔH_{mix} (kJ/mol), ΔS_{mix} (J/mol·K), ΔG_{mix} (kJ/mol) at temperature T (K), parameters δ_a and δ_c, and comparison of theoretical and experimental lattice parameters (Å) of $(Hf_xZr_{1-x})B_2$

Solid solution		$(Hf_{0.2}Zr_{0.8})B_2$	$(Hf_{0.5}Zr_{0.5})B_2$	$(Hf_{0.8}Zr_{0.2})B_2$
a (Å)	Cal.	3.168	3.159	3.149
	Vegard Law	3.164	3.156	3.148
	Exp.	3.162	3.155	3.146
c (Å)	Cal.	3.543	3.523	3.503
	Vegard Law	3.520	3.503	3.487
	Exp.	3.518	3.503	3.484
δ_a (%)		0.315	0.400	0.348
δ_c (%)		0.628	0.790	0.590
ΔH_{mix} (kJ/mol)		−0.384	−0.108	−0.493
ΔS_{mix} (J/(mol·K))		4.154	5.762	4.154
ΔG_{mix} (kJ/mol)		−0.384–4.154×10^{-3} T	−0.108–5.762×10^{-3} T	−0.493–4.154×10^{-3} T

diboride constituent, respectively. $\bar{r}$ is defined as the average lattice size of the actual lattice parameters of different diboride ceramics. The slightly higher δ_a (0.400%) and δ_c (0.790%) of $(Hf_{0.5}Zr_{0.5})B_2$ indicate a modest increase in lattice distortion.

The mixing enthalpy (ΔH_{mix}) in high-entropy ceramic systems provides a quantitative assessment of their solid solution formation capability, which is evaluated via DFT using Eq. (4) [39]:

$$\Delta H_{mix} = E_{total}(\text{supercell}) - \sum c_i E_i \quad (4)$$

where c_i represents the proportion of the i-th constituent, E_{total}(supercell) denotes the energy per atom of the boride solid solution supercell, and E_i is the energy per atom of the i-th diboride constituent. ΔH_{mix} is associated with the interplay of multiple factors, including lattice distortion arising from atomic size mismatch, differences in charge transfer and electronic structure [40]. The calculated ΔH_{mix} values of $(Hf_{0.2}Zr_{0.8})B_2$, $(Hf_{0.5}Zr_{0.5})B_2$, and $(Hf_{0.8}Zr_{0.2})B_2$ are −0.384, −0.108, and −0.493 kJ/mol, respectively. The larger value of ΔH_{mix} for $(Hf_{0.2}Zr_{0.8})B_2$ and $(Hf_{0.5}Zr_{0.5})B_2$ reveals their inferior solid solution formation tendency, which requires higher synthesis temperatures (1800 and 1900 °C, respectively, Fig. 2) to achieve a single-phase structure. In contrast, the more negative ΔH_{mix} value for $(Hf_{0.8}Zr_{0.2})B_2$ confirms a thermodynamically favorable tendency, which is consistent with their lower single-phase formation temperature (1700 °C, Fig. 2). The thermodynamic stability of the solid solution was further evaluated by calculating the mixing Gibbs free energy (ΔG_{mix}), given by Eqs. (5) and (6) [41]:

$$\Delta G_{mix} = \Delta H_{mix} - T\Delta S_{mix} \quad (5)$$

$$\Delta S_{mix} = -R[x \ln x + (1-x)\ln(1-x)] \quad (6)$$

where the configurational entropy is defined as ΔS_{mix}, which arises solely from the random mixing of Hf and Zr atoms on the A-sublattice of the AB_2 structure, R is the ideal gas constant, and x is the mole fraction of Hf atoms on the A-sublattice. As listed in Table 2, $(Hf_{0.8}Zr_{0.2})B_2$ exhibits the most negative ΔG_{mix} across nearly the entire temperature range, indicating its superior thermodynamic stability, while $(Hf_{0.5}Zr_{0.5})B_2$ is the least stable. This is completely consistent with the results of ΔH_{mix}.

Furthermore, the DFT-derived lattice parameters show good agreement with Vegard's law and experimental values obtained from XRD refinement, which are intermediate between those of HfB_2 (a = 3.143 Å, c = 3.476 Å) and ZrB_2 (a = 3.169 Å, c = 3.531 Å), indicating that the synthesized solid solution powders possess the expected geometric structures by UHS technology.

The formation of solid solutions involves the substitution of Hf and Zr atoms on the cation sublattice. To quantitatively understand the varying formation tendencies, the solution energy (E_{sol}) was calculated, which represents the required energy for a transition metal atom from the unit cell to replace a host atom in the parent lattice [42]. This parameter serves as an indicator of the driving force for the dissolution of the Hf-rich phase into Zr-rich host lattices, or vice versa, during high-temperature processing (Fig. 6(a)), which is beneficial for explaining the varying tendency for single-phase $(Hf_xZr_{1-x})B_2$ formation. The solution energy is defined as Eq. (7) [43]:

$$E_{sol} = E_{MB_2-N_{sol}} + E_M - E_{MB_2} - E_N \quad (7)$$

where $E_{MB_2-N_{sol}}$ stands for the total energy of the host supercell structure (HfB_2 or ZrB_2) with solution atoms N, E_{MB_2} is the energy of the pristine host supercell structure, E_M represents the energy of the boride unit cell containing the substituted atom, and E_N denotes the energy of the boride unit cell containing the substituting atom. As shown in Fig. 6(b), a lower E_{sol} (Zr → HfB_2(supercell)) than E_{sol} (Hf → ZrB_2(supercell)) indicates that Zr is incorporated more readily into HfB_2 than the reverse. This trend aligns with the lattice mismatch parameter δ in Table 1 and explains why $(Hf_{0.8}Zr_{0.2})B_2$ forms more readily under UHS processing, while single-phase $(Hf_{0.2}Zr_{0.8})B_2$ is more challenging to synthesize.

The density of states (DOS) represents the number of electrons allowed per unit energy, which can reflect the essential electronic properties [44]. Figures 6(c)–6(e) present the partial and total DOS curves for the three boride solid solutions. The total DOS of $(Hf_xZr_{1-x})B_2$ is mainly contributed by B-2s and 2p, Hf-5d, and Zr-4d states. Near the Fermi level (E_f, black vertical dashed lines), the DOS is primarily dominated by the B-2p and metal-d states. The DOS values at E_f for $(Hf_{0.2}Zr_{0.8})B_2$, $(Hf_{0.5}Zr_{0.5})B_2$, and $(Hf_{0.8}Zr_{0.2})B_2$ are 1.47, 2.91, and 1.42 electrons/eV, respectively. Nonzero DOS values at E_f imply that the $(Hf_xZr_{1-x})B_2$ ceramics possess metal characteristics, and the higher number of bonding electrons at E_f for $(Hf_{0.5}Zr_{0.5})B_2$ represents its lower stability. Consequently, the phase stability increases in the order of $(Hf_{0.5}Zr_{0.5})B_2$ < $(Hf_{0.2}Zr_{0.8})B_2$ < $(Hf_{0.8}Zr_{0.2})B_2$, consistent with the calculated results of ΔH_{mix} and ΔG_{mix}.

To comprehensively investigate the electronic structure and charge transfer behavior of $(Hf_xZr_{1-x})B_2$, we calculated the electron localization function (ELF) and average length. Referring to Fig. 6(a), the (110) and (001) planes were selected for ELF analysis to specifically probe the chemical bonding environments of B–B and M–B bonds, considering that the (110) plane intersects complete B layers, while the (001) plane cuts across alternating Hf/Zr and B layers. The ELF of $(Hf_{0.5}Zr_{0.5})B_2$ is displayed as representative, as shown in Fig. 7(a). The reddish orange regions between adjacent B atoms on the (110) plane signify strong electron localization, indicating strong covalent bonding between boron atoms. The blue regions around the Hf and Zr atoms in the (110) plane indicate a highly delocalized electron distribution around transition metal atoms. The Bader charge quantifies the charge transfer from transition metal atoms to boron atoms, and the calculated values confirm that Hf atoms contribute more electrons to bond with B atoms [45]. The ELF results reveal that the stability of the boride solid solutions is primarily due to the

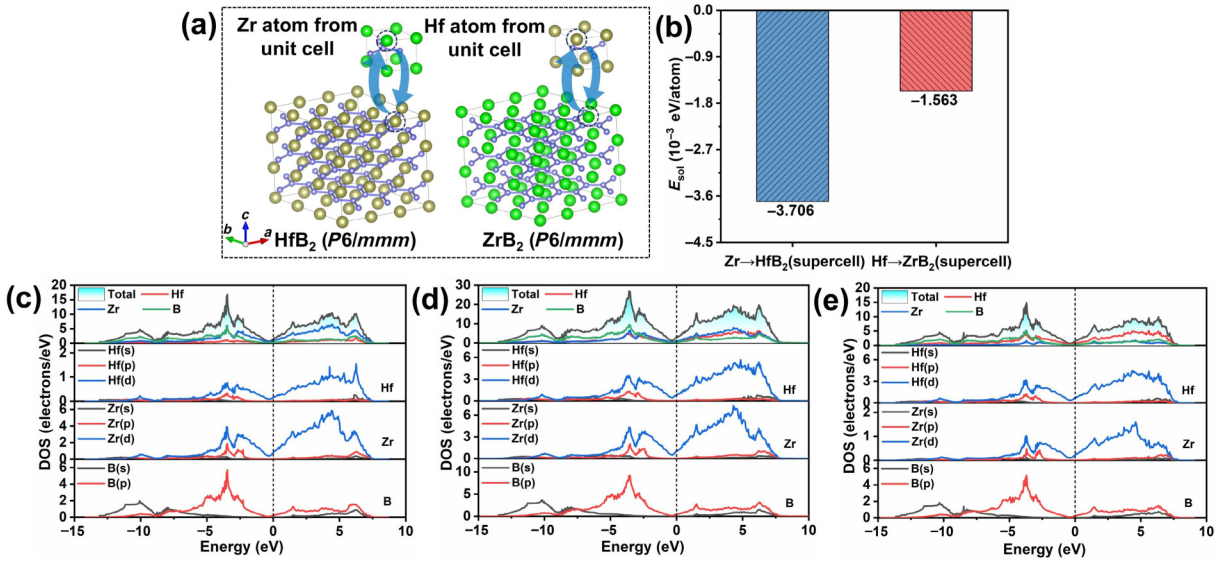

Fig. 6 First-principles calculations: (a) solution model of HfB_2 and ZrB_2; (b) E_{sol} of Hf and Zr atoms from the unit cell, and the total and partial density of states of (c) $(Hf_{0.2}Zr_{0.8})B_2$, (d) $(Hf_{0.5}Zr_{0.5})B_2$, and (e) $(Hf_{0.8}Zr_{0.2})B_2$ ceramics. The Fermi level is represented by a vertical dashed line.

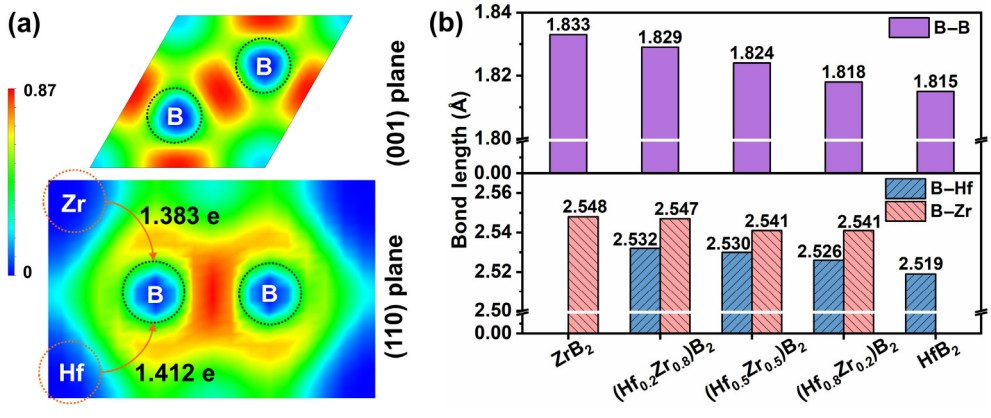

Fig. 7 ELF contour of $(Hf_{0.5}Zr_{0.5})B_2$ ideal solid solution ceramics on the (001) and (110) planes (numbers at the arrows indicate (a) the Bader charges on the (110) plane) and (b) average bond length of B–B, B–Hf, and B–Zr in $(Hf_xZr_{1-x})B_2$.

contribution of B–B covalent bonds. As shown in Fig. 7(b), the B–B bond lengths decrease with increasing Hf content. Zr–B bonds are longer than Hf–B bonds due to the stronger electronic hybridization of the latter, indicating that a higher Zr content weakens the overall bonding network. $(Hf_{0.8}Zr_{0.2})B_2$ exhibits reduced bond lengths (2.526 Å for Hf–B, 2.541 Å for Zr–B and 1.818 Å for B–B), correlating well with its superior phase stability.

4 Conclusions

In this work, $(Hf_xZr_{1-x})B_2$ (x = 0.2, 0.5, 0.8) nanopowders were successfully synthesized via UHS. The rapid heating rate effectively suppresses grain growth, resulting in nanoscale particle sizes below 500 nm with a well-defined hexagonal AlB_2-type structure. First-principles calculations indicate a lower E_{sol} for Zr atoms entering the HfB_2 lattice than the reverse process, which is consistent with the lower synthesis temperature required for single-phase $(Hf_{0.8}Zr_{0.2})B_2$ (1700 °C) compared to $(Hf_{0.5}Zr_{0.5})B_2$ (1800 °C) and $(Hf_{0.2}Zr_{0.8})B_2$ (1900 °C), indicating a stronger formation tendency for Hf-rich composition. In addition to its higher formation propensity, $(Hf_{0.8}Zr_{0.2})B_2$ also exhibits optimal stability from both phase and thermodynamic perspectives, as evidenced by its more negative ΔG_{mix}, lower DOS value at E_f, and shorter average bond length. In contrast, excessive Zr introduces a higher fraction of weakened covalent Zr–B bonds, resulting in diminished stability of the solid solution. This work provides valuable insights for the compositional regulation and efficient synthesis of multiboride nanopowders.

Acknowledgements

This work has been supported by the National Natural Science Foundation of China (Grant Nos. 52402113 and 52302091), the Joint Fund of Henan Province Science and Technology R&D Program (Grant Nos. 235200810072, 235200810094, and 245200810094), Henan Province Major Basic Research Program (Grant No. 252310420100), and the Scientific and Technological Research Project of Henan Academy of Sciences (Grant No. 20252321002).

Availability of data and materials

The data are available from the corresponding author upon reasonable request.

Competing interests

The authors have no competing interests to declare that are relevant to the content of this article.

References

[1] Chen H, Zhang YL, Fu YQ, *et al.* Novel $Hf_xTa_{1-x}C$ solid solution

nanowire toughened HfC coating: An effective strategy for synchronous enhanced mechanical and anti-ablation performance. *J Adv Ceram* 2024, **13**: 590–601.
[2] Li JC, Lu FY, Li T, *et al.* Superior synergistic oxidation resistance of medium-entropy carbide ceramic powders rather than multi-phase carbide ceramic powders. *J Adv Ceram* 2024, **13**: 1223–1233.
[3] Li JC, Li T, Huang CJ, *et al.* The synergistic effect of multi-phase oxides on the ablation resistance of TaC-modified HfC–ZrC coatings for C/C composites. *Corros Sci* 2024, **228**: 111795.
[4] Li JC, Zhang YL, Fu YQ, *et al.* Twin toughening-driven martensitic transformation strategy synergistic improvement for plasticity-thermal shock resistance of (Hf–Zr–Ti)C ceramic coating in severe thermal environments. *Adv Sci* 2025, **12**: 2503226.
[5] Fu YQ, Zhang YL, Yan H, *et al.* Microstructure and evolution of hafnium carbide whiskers via polymer-derived ceramics: A novel formation mechanism. *J Adv Ceram* 2023, **12**: 578–586.
[6] Zhang JH, Fu YQ, Lv JS, *et al.* Tailoring ablation resistance of (Hf,Zr,Ta)C coatings above 2000 ℃: Critical role of Ta content. *J Adv Ceram* 2026, **15**: 9221207.
[7] Zhao JH, Zhang YL, Chen H, *et al.* Single-source precursor derived high-entropy metal–carbide nanowires: Microstructure and growth evolution. *J Adv Ceram* 2023, **12**: 2041–2052.
[8] Golla BR, Mukhopadhyay A, Basu B, *et al.* Review on ultra-high temperature boride ceramics. *Prog Mater Sci* 2020, **111**: 100651.
[9] Lv JS, Li W, Li T, *et al.* Multicomponent (Hf–Zr–Ta)B_2 coatings for carbon/carbon composites and structural optimization enabling superior ablation resistance. *J Mater Sci Technol* 2025, **204**: 115–126.
[10] Lv JS, Li W, Fu YQ, *et al.* Functionally graded oxide scale on (Hf,Zr,Ti)B_2 coating with exceptional ablation resistance induced by unique Ti dissolving. *Adv Sci* 2025, **12**: 2411292.
[11] Li HJ, Yao DJ, Fu QG, *et al.* Anti-oxidation and ablation properties of carbon/carbon composites infiltrated by hafnium boride. *Carbon* 2013, **52**: 418–426.
[12] Zhang P, Cheng CY, Xu M, *et al.* High-entropy $(Hf_{0.25}Zr_{0.25}Ti_{0.25}Cr_{0.25})B_2$ ceramic incorporated SiC–Si composite coating to protect C/C composites against ablation above 2400 K. *Ceram Int* 2022, **48**: 27106–27119.
[13] Ji X, Zhao J, Ren XR, *et al.* Thermal expansion mismatch-induced *in situ* self-assembly design of gradient coatings: 1700 °C oxidation protection and oxygen barrier enhancement mechanism of borosilicate-modified ZrB_2–$MoSi_2$–BSG gradient composite coatings. *Corros Sci* 2026, **260**: 113581.
[14] Liu D, Wen TQ, Ye BL, *et al.* Molten salt synthesis, characterization, and formation mechanism of superfine $(Hf_xZr_{1-x})B_2$ solid-solution powders. *J Am Ceram Soc* 2019, **102**: 3763–3770.
[15] Gai WH, Zhang YL, Chen H, *et al.* Controllable growth of (Hf,Zr)B_2 solid solution coating *via* CVD for ultra-high temperature ablation of C/C composites. *J Eur Ceram Soc* 2024, **44**: 2821–2830.
[16] Hassan R, Omar S, Balani K. Solid solutioning in ZrB_2 with HfB_2: Effect on densification and oxidation resistance. *Int J Refract Met Hard Mater* 2019, **84**: 105041.
[17] Liu YW, Ma MD, Wang W, *et al.* Lattice distortion enhanced hardness in high-entropy borides. *Adv Funct Mater* 2025, **35**: 2416992.
[18] Zhao XT, Wang HL, Shao G, *et al.* Processing and properties of (Zr,Hf)B_2–SiC ceramic composites. *Solid State Phenom* 2018, **281**: 438–443.
[19] Lv JS, Li W, Li T, *et al.* Ablation behavior of high-entropy boride (Hf–Zr–Ta–Ti)B_2 coating fabricated via supersonic atmospheric plasma spraying for carbon/carbon composites. *Compos Part B Eng* 2024, **270**: 111137.
[20] Zamora V, Ortiz AL, Guiberteau F, *et al.* Crystal-size dependence of the spark-plasma-sintering kinetics of ZrB_2 ultra-high-temperature ceramics. *J Eur Ceram Soc* 2012, **32**: 271–276.
[21] Backman L, Gild J, Qin MD, *et al.* Composition dependence of oxidation resistance in high entropy ultra-high temperature ceramics. *Open Ceram* 2024, **18**: 100563.
[22] Castle E, Csanádi T, Grasso S, *et al.* Processing and properties of high-entropy ultra-high temperature carbides. *Sci Rep* 2018, **8**: 8609.
[23] Silvestroni L, Gilli N, Sangiorgi A, *et al.* Multi-phase (Zr,Ti,Cr)B_2 solid solutions: Preparation, multi-scale microstructure, and local properties. *J Adv Ceram* 2023, **12**: 414–431.
[24] Zhang ML, Ren XR, Zhang MC, *et al.* Preparation of ZrB_2–$MoSi_2$ high oxygen resistant coating using nonequilibrium state powders by self-propagating high-temperature synthesis. *J Adv Ceram* 2021, **10**: 1011–1024.
[25] Shao ZJ, Zeng DW, Xu MJ, *et al.* A novel highly porous dual-phase high-entropy ultrahigh-temperature ceramic with outstanding properties. *J Adv Ceram* 2025, **14**: 9221132.
[26] Wang CW, Ping WW, Bai Q, *et al.* A general method to synthesize and sinter bulk ceramics in seconds. *Science* 2020, **368**: 521–526.
[27] Xie H, Qin MD, Hong M, *et al.* Rapid liquid phase–assisted ultrahigh-temperature sintering of high-entropy ceramic composites. *Sci Adv* 2022, **8**: eabn8241.
[28] Tang ZY, Wen ZH, Liu YW, *et al.* Rapid experimental screening of high-entropy diborides for superior oxidation resistance. *Adv Funct Mater* 2024, **34**: 2312239.
[29] Xu YX, Yu L, Zhao T, *et al.* Composition design of oxidation resistant non-equimolar high-entropy ceramic materials: An example of (Zr–Hf–Ta–Ti)B_2 ultra-high temperature ceramics. *J Adv Ceram* 2024, **13**: 2087–2100.
[30] Wen ZH, Meng H, Jiang SD, *et al.* Non-equimolar (Hf,Zr,Ta,W)B_2 high-entropy diborides enable superior oxidation resistance. *Sci China Mater* 2023, **66**: 3213–3222.
[31] Guo WM, Yang ZG, Zhang GJ. Synthesis of submicrometer HfB_2 powder and its densification. *Mater Lett* 2012, **83**: 52–55.
[32] Liu D, Wen TQ, Ye BL, *et al.* Synthesis of superfine high-entropy metal diboride powders. *Scr Mater* 2019, **167**: 110–114.
[33] Qin Y, Zhang ZG, Liang WJ, *et al.* Study on the effect of temperature and pressure environments on the mechanical and electronic properties of titanium carbon nitride ceramics. *ACS Appl Mater Interfaces* 2025, **17**: 1556–1564.
[34] Sun WG, Kuang XY, Liang H, *et al.* Mechanical properties of tantalum carbide from high-pressure/high-temperature synthesis and first-principles calculations. *Phys Chem Chem Phys* 2020, **22**: 5018–5023.
[35] Zhang ZG, Wu JS, Zhu Q, *et al.* A method probing high-temperature oxidation behavior of crystalline materials. *Small* 2024, **20**: 2308718.
[36] Bish DL, Howard SA. Quantitative phase analysis using the Rietveld method. *J Appl Crystallogr* 1988, **21**: 86–91.
[37] Zhang Y, Sun SK, Zhang W, *et al.* Improved densification and hardness of high-entropy diboride ceramics from fine powders synthesized via borothermal reduction process. *Ceram Int* 2020, **46**: 14299–14303.
[38] Guo LX, Huang SW, Li W, *et al.* Theoretical design and experimental verification of high-entropy carbide ablative resistant coating. *Adv Powder Mater* 2024, **3**: 100213.
[39] Qi W, Chen B, Yang X, *et al.* Phase stability, mechanical and thermodynamic properties of (Hf,Zr,Ta,M)B_2 (M = Nb, Ti, Cr, W) quaternary high-entropy diboride ceramics *via* first-principles calculations. *Ceram Int* 2023, **49**: 33255–33264.
[40] Liu Z, Zhang LQ. Phase formation criteria for structurally ordered high-entropy intermetallics. *J Alloys Compd* 2024, **981**: 173716.
[41] Guo LX, Wang YQ, Liu B, *et al.* *In-situ* phase evolution of multi-component boride to high-entropy ceramic upon ultra-high temperature ablation. *J Eur Ceram Soc* 2023, **43**: 1322–1333.
[42] Xie W, Fu QG, Cheng CY, *et al.* Experimental and theoretical study on the effect of different rare-earth oxides on the high-temperature stability of SiO_2 glass at 1973K. *Ceram Int* 2020, **46**: 24371–24378.
[43] Li HS, Cao Y, Zhou SG, *et al.* Site preferences and effects of X (X = Mn, Fe, Co, Cu) on the properties of NiAl: A first-principles study. *Mod Phys Lett B* 2016, **30**: 1650133.
[44] Zhang Z, Zhu SZ, Liu YB, *et al.* Enthalpy driving force and chemical bond weakening: The solid-solution formation mechanism and densification behavior of high-entropy diborides $(Hf_{1-x}/4Zr_{1-x}/4Nb_{1-x}/4Ta_{1-x}/4Sc_x)B_2$. *J Eur Ceram Soc* 2022, **42**: 3685–3698.
[45] Vajeeston P, Ravindran P, Ravi C, *et al.* Electronic structure, bonding, and ground-state properties of AlB_2-type transition-metal diborides. *Phys Rev B* 2001, **63**: 045115.